Hindawi Publishing Corporation
International Journal of Photoenergy
Volume 2013, Article ID 484831, 9 pages
http://dx.doi.org/10.1155/2013/484831

Research Article

Kinetics Study of Photocatalytic Activity of Flame-Made Unloaded and Fe-Loaded CeO_2 Nanoparticles

D. Channei,[1] B. Inceesungvorn,[1] N. Wetchakun,[2] and S. Phanichphant[3]

[1] *Department of Chemistry, Faculty of Science, Chiang Mai University, Chiang Mai 50200, Thailand*
[2] *Department of Physics and Materials Science, Faculty of Science, Chiang Mai University, Chiang Mai 50200, Thailand*
[3] *Materials Science Research Center, Faculty of Science, Chiang Mai University, Chiang Mai 50200, Thailand*

Correspondence should be addressed to S. Phanichphant; sphanichphant@yahoo.com

Received 8 June 2013; Accepted 4 October 2013

Academic Editor: Jiaguo Yu

Unloaded CeO_2 and nominal 0.50, 1.00, 1.50, 2.00, 5.00, and 10.00 mol% Fe-loaded CeO_2 nanoparticles were synthesized by flame spray pyrolysis (FSP). The samples were characterized to obtain structure-activity relation by X-ray diffraction (XRD), high-resolution transmission electron microscopy (HRTEM), Brunauer, Emmett, and Teller (BET) nitrogen adsorption, X-ray photoelectron spectroscopy (XPS), and UV-visible diffuse reflectance spectrophotometry (UV-vis DRS). XRD results indicated that phase structures of Fe-loaded CeO_2 nanoparticles were the mixture of CeO_2 and Fe_2O_3 phases at high iron loading concentrations. HRTEM images showed the significant change in morphology from cubic to almost-spherical shape observed at high iron loading concentration. Increased specific surface area with increasing iron content was also observed. The results from UV-visible reflectance spectra clearly showed the shift of absorption edge towards longer visible region upon loading CeO_2 with iron. Photocatalytic studies showed that Fe-loaded CeO_2 sample exhibited higher activity than unloaded CeO_2, with optimal 2.00 mol% of iron loading concentration being the most active catalyst. Results from XPS analysis suggested that iron in the Fe^{3+} state might be an active species responsible for enhanced photocatalytic activities observed in this study.

1. Introduction

Organic compounds from industries are one of the major causes of water pollution [1]. Various strategies have been employed to remove these toxic compounds [2, 3]. One of the most interesting approaches is heterogeneous photocatalysis because the process is based on the use of solar energy, which is clean and abundant in nature [4, 5]. In the recent years, cerium dioxide (CeO_2 or ceria) has received considerable attention because this material shows promising applications in solid oxide fuel cells [6], environmental catalysis [7, 8], redox catalysis [9], and wet catalytic oxidation of organic pollutants [10]. However, the band gap of CeO_2 (3.22 eV) has limited the activation of solar energy; only UV light can be applied to generate electron-hole pairs at the beginning of photocatalytic processes. Thus, it is necessary to extend the absorbance of CeO_2 into visible region and reduce the electron-hole pairs recombination [11, 12]. There are many methods to modify light absorption properties of CeO_2, such as metal doping [13, 14], surface sensitization [15], and coupling with semiconductor that has smaller band gap [16]. Recently, transition metal doping/loading has been widely used to enhance the light absorption of CeO_2 [17, 18]. It has been reported in many works of literature that the metal ions of Pt [19], Ag [20], Fe [21], Mn [22], Co [23], Ni [24], and Zn [25] in CeO_2 could improve CeO_2 photocatalytic activity towards the visible-light region. Among these metals, Fe has been considered as a candidate owing to its special Fenton reaction of iron. The Fenton process can improve the photocatalytic activity by producing the hydroxyl radicals ($OH^{\bullet}$) which are very powerful oxidizer in photocatalytic process [26]. There are many methods to prepare unloaded CeO_2 and Fe-doped/-loaded CeO_2 nanoparticles such as sol-gel [27], sonochemical [28], homogeneous precipitation [29], hydrothermal [30], microemulsions [31], surfactant-assisted precipitation [32], and flame spray pyrolysis (FSP) methods [33].

Among them, the latter one is a promising approach because FSP can produce the nanoparticle products with particle size in the range of 1–200 nm at high production rates up to 250 g/h in one step [34]. Other advantages are the ability to dissolve the precursor directly in the fuel and the simplicity of introduction of the precursor into the hot flame zone. In addition, the process of loading/doping metal oxide with metals can easily be done by adding dopant in the precursor solution [35, 36]. In the present work, unloaded CeO_2 and Fe-loaded CeO_2 nanoparticles were directly synthesized by FSP method. The formic acid and oxalic acid were chosen as model organic pollutants for photocatalytic study under visible-light irradiation.

2. Experimental

2.1. Preparation of Powders. The precursor solutions for FSP consisted of cerium nitrate hexahydrate (Sigma-Aldrich, 99.99 wt%) and iron acetyl acetonate (Sigma-Aldrich, 97 wt%). The cerium precursor was dissolved in absolute ethanol (Scharlau, 98%) to obtain a 0.50 M concentration. Amounts of Fe loading concentration were varied as 0.50, 1.00, 1.50, 2.00, 5.00, and 10.00 mol% in order to prepare Fe-loaded CeO_2 samples. The precursor mixtures were fed into the center of flame by syringe pump with a rate of 5 mL/min and dispersed by 5 L/min oxygen according to the previous report [37]. Then, the liquid precursor was dispersed quickly in an upward direction by gas stream and ignited by premixed oxygen/methane flame. The gas flow rates of oxygen and methane-supporting flame were set as constant rates of 1.19 and 2.46 L/min, respectively. After evaporation and combustion of liquid precursor droplet, nanoparticle products were collected on a glass microfiber filter papers (Whatmann GF/A, 25.7 cm in diameter) with a vacuum pump controller.

2.2. Characterization of Nanoparticles. The phase and crystallinity of the synthesized samples were analyzed by X-ray powder diffraction (XRD; Philips X'Pert MPD; CuKα radiation). The most intense peak corresponding to (111) plane was chosen to calculate the crystallite sizes (D) using Scherrer equation as follow:

$$D = \frac{k\lambda}{\beta \cos\theta}, \quad (1)$$

where k is a constant equal to 0.89, λ is the X-ray wavelength equal to 0.154 nm, β is the full width at half-maximum (FWHM), and θ is the half-diffraction angle [38]. The chemical composition and oxidation state of material were studied by X-ray photoelectron spectroscopy (XPS) using Mg X-ray source (MgKα, Kratos Axis Ultra DLD). The binding energy of the adventitious carbon (C 1s) line at 285 eV was used for calibration, and the position of other peaks was corrected according to the position of the C 1s signal. High-resolution transmission electron microscopy (HRTEM, JEOL JEM-2010) was employed to determine the morphology of prepared samples. The mean particle size and specific surface area (SSA) were investigated using the Brunauer, Emmett, and Teller (BET) nitrogen adsorption method (Quantachrome Autosorp 1 MP). The reflectance spectra of the nanoparticle powders were obtained by using UV-visible diffuse reflectance spectrophotometry (UV-vis DRS) equipped with integrating sphere detector (Shimadzu, UV-3101PC).

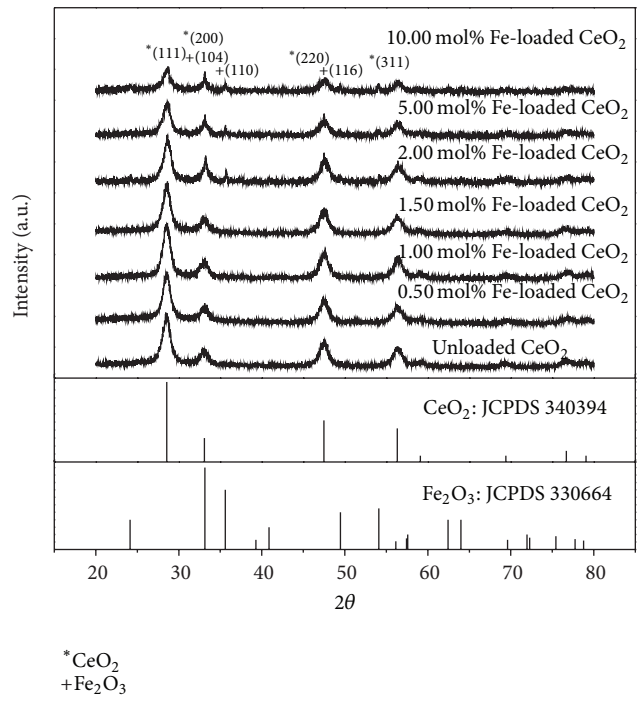

Figure 1: X-ray diffraction patterns of CeO_2 with different iron content.

2.3. Photocatalytic Activity. 1.00 g /L of photocatalyst suspensions was prepared in deionized water and circulated in closed system spiral photoreactor. In a typical run, carbon burn-off step was firstly carried out by illuminating the photocatalyst suspension with a UV-A lamp (Sylvania Blacklight Blue, 18 W) in order to remove any organic impurities from the photocatalyst. The photocatalytic activities were evaluated through formic acid (Sigma-Aldrich, 98 wt%) and oxalic acid (Sigma-Aldrich, 99.99 wt%) degradations under the visible irradiation for 120 min. Finally, the generated carbon dioxide (CO_2) was measured using the conductivity meter (Eutech Instruments Cyberscan PC5500, μS/cm^2 precision). At the end of each photocatalytic experiment, the recorded data presented the increase in conductivity value. In order to calculate amounts of generated CO_2, the values were converted from conductivity at that time to the amount of carbon by the interpolated from calibration curve.

3. Results and Discussion

3.1. X-Ray Powder Diffraction (XRD). In Figure 1, the X-ray diffraction pattern has been used in order to study the structure and phase composition of the prepared samples. It can be seen that all samples had similar diffraction patterns of cubic fluorite structure of ceria (JCPDS 340394) [39]. However,

Table 1: The calculated d-spacing, lattice parameters, unit cell volume, and crystalline size.

Iron loading concentration (mol%)	111 plane				
	2θ (degree)	d-spacing (nm)	Lattice parameter (nm)	Unit cell volume (nm^3)	Crystalline size (nm)
0.00	28.4601	0.3132	0.5426	0.1597	8.3586
0.50	28.5479	0.3123	0.5409	0.1583	7.8555
1.00	28.5699	0.3121	0.5405	0.1579	7.4111
1.50	28.5772	0.3120	0.5404	0.1578	7.4081
2.00	28.6284	0.3114	0.5394	0.1570	6.9682
5.00	28.6490	0.3112	0.5390	0.1566	6.2226
10.00	28.7098	0.3106	0.5380	0.1557	5.7476

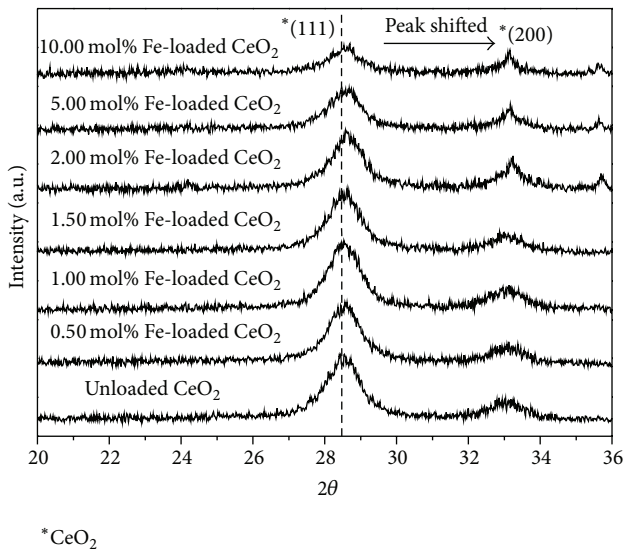

Figure 2: The shift of 2θ of samples.

the sample with high amount of iron loading (2.00, 5.00, and 10.00 mol%) exhibited the mixed phase of CeO_2 and Fe_2O_3 (JCPDS 330664) [40]. The XRD peaks of all samples were magnified as shown in Figure 2. It was found that CeO_2 peaks shifted towards higher 2θ upon increasing iron content. The calculated d-spacing, lattice parameter, unit cell volume, and average crystallite size were also decreased as shown in Table 1. These observations could be ascribed to partial substitution of Ce^{4+} ions (0.101 nm) by Fe^{3+} ions (0.064 nm) [41]. A decrease of unit cell parameters due to the substitution of larger ion by the smaller one was also found in previous reports [42, 43].

3.2. High-Resolution Transmission Electron Microscopy (HRTEM). As seen from Figure 3(a), the unloaded CeO_2 clearly showed the cubic morphology of cubic fluorite CeO_2 structure. In Figure 3(b), the particles became more spherical upon loading CeO_2 with iron. This change in CeO_2 morphology might be due to the incorporation of iron ions in CeO_2 lattice, thus affecting the particle growth and causing lattice deformation [44]. This assumption was supported by the shift of XRD peak and the changes of lattice parameters as reported in Table 1. The average particle sizes as seen from HRTEM image were about 6–8 nm. This was in good agreement with the calculated sizes obtained by using the Scherrer equation. Figure 3(c) shows the lattice fringes of 2.00 mol% Fe-loaded CeO_2. The lattice planes with d-spacing of 0.16 and 0.20 nm were attributed to the (311) and (220) planes of cubic fluorite CeO_2, respectively, whereas the plane with d-spacing of 0.24 was assigned to the (110) plane of Fe_2O_3. These results confirmed the presence of mixed phase between CeO_2 and Fe_2O_3 in the nominal 2.00 mol% Fe-loaded CeO_2 as found previously in the XRD patterns (Figure 1).

Table 2: Summary of analytical data.

Iron loading concentration (mol%)	SSA (m^2/g)	E_g (eV)	BET diameter (nm)
0	130.00	3.21	6.39
0.50	134.00	2.95	6.20
1.00	137.97	2.70	6.02
1.50	137.99	2.65	6.02
2.00	139.00	2.55	5.98
5.00	140.82	2.45	5.57
10.00	148.76	2.35	5.27

3.3. Nitrogen Adsorption-Desorption Isotherms. The specific surface areas (SSA) of different samples were analyzed by Brunauer-Emmett-Teller (BET) method based on the nitrogen adsorption/desorption isotherm. The mean BET diameter (D) was also calculated by using the following equation [45]:

$$D = \frac{6000}{\left(S_{\mathrm{BET}} \times \rho\right)}, \tag{2}$$

where S_{BET} is the BET-specific surface area and ρ is the density of the CeO_2 (7.32 g/mL). As shown in Table 2, an increase of surface area accompanied with a decrease of BET diameter was clearly observed upon increasing iron content. This increased surface area would be beneficial to the efficient photocatalytic performance due to high surface adsorption of organic pollutants. The calculated BET diameter was in

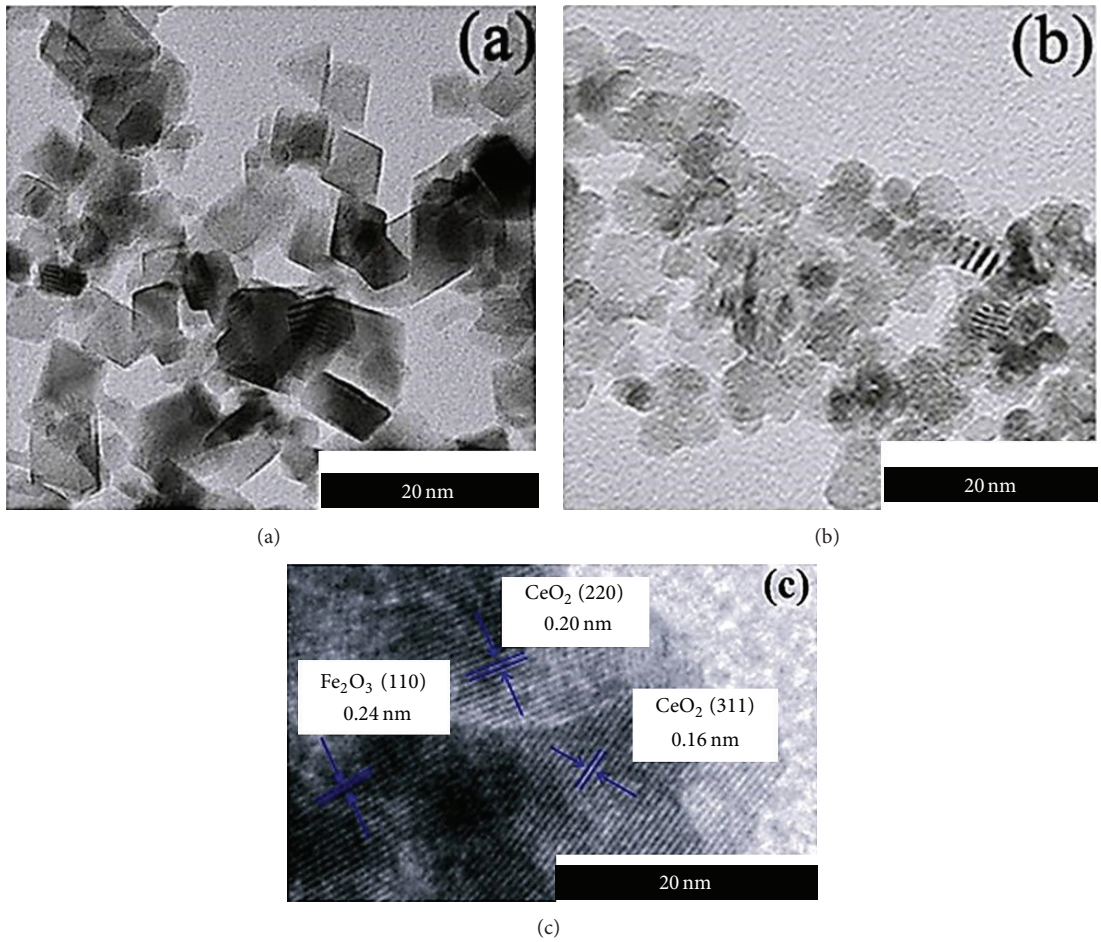

Figure 3: HRTEM images of (a) unloaded CeO_2, (b) 2.00 mol% Fe-loaded CeO_2, and (c) lattice fringe of 2.00 mol% Fe-loaded CeO_2.

the range of 5–7 nm which was very well in agreement with those obtained by using the Scherrer equation (Table 1).

3.4. UV-Visible Spectroscopy. UV-vis reflectance analysis was performed by converting the obtained reflectance spectra (Figure 4(a)) to the Kubelka-Munk absorbance spectra using the Kubelka-Munk equation as follows [46]:

$$F\left(R_\infty\right) = \frac{\left(1 - R_\infty\right)^2}{2R_\infty}, \tag{3}$$

where $F(R_\infty)$ and R_∞ are the Schuster-Kubelka-Munk absorbance and the absolute reflectance of the sample, respectively. The plot of absorbance against wavelength for the CeO_2 nanoparticle powders is shown in Figure 4(b).

The spectra showed that the absorption edge shifted to longer wavelength upon increasing the iron loading concentration. Band gap energies of the obtained samples can then be determined by using the intercept of the tangent to the graph plotting between the Kubelka-Munk absorption function and photon energy ($h\nu$) as shown in Figure 4(c) [47, 48]. The obtained band gap energies (E_g) as reported in Table 2 decreased with increasing iron loading concentration.

3.5. Photocatalytic Activity. The photocatalytic activity of unloaded and Fe-loaded CeO_2 was evaluated by degradation of formic and oxalic acids. The effects of different iron loading concentrations on the photocatalytic efficiency of CeO_2 nanoparticles were evaluated under visible-light irradiation for 120 min, and the results are presented in Figure 5. According to the results, the photocatalytic activities of Fe-loaded CeO_2 nanoparticles were significantly higher than those of unloaded CeO_2 nanoparticles. This improved photoactivity could be partially ascribed to the enhanced light absorption in visible-light region as observed from the UV-vis study in Figure 4. However, the activity was clearly dependent on the amount of iron loading. The results demonstrated that the nominal 2.00 mol% was an optimal iron concentration for photocatalytic activity of CeO_2 nanoparticles in this research. On the other hand, 5.00% and 10.00 mol% iron concentrations showed poor photocatalytic activity, probably because high iron concentration tended to cover CeO_2 surface, thus preventing light from contacting the CeO_2 surface [49].

Another possible reason was that too high iron loading can act as the electron-hole recombination centers instead of the trapping level, resulting in a decreased photocatalytic activity [47, 50]. The kinetic data for formic and oxalic acids degradations under visible-light illumination were found to

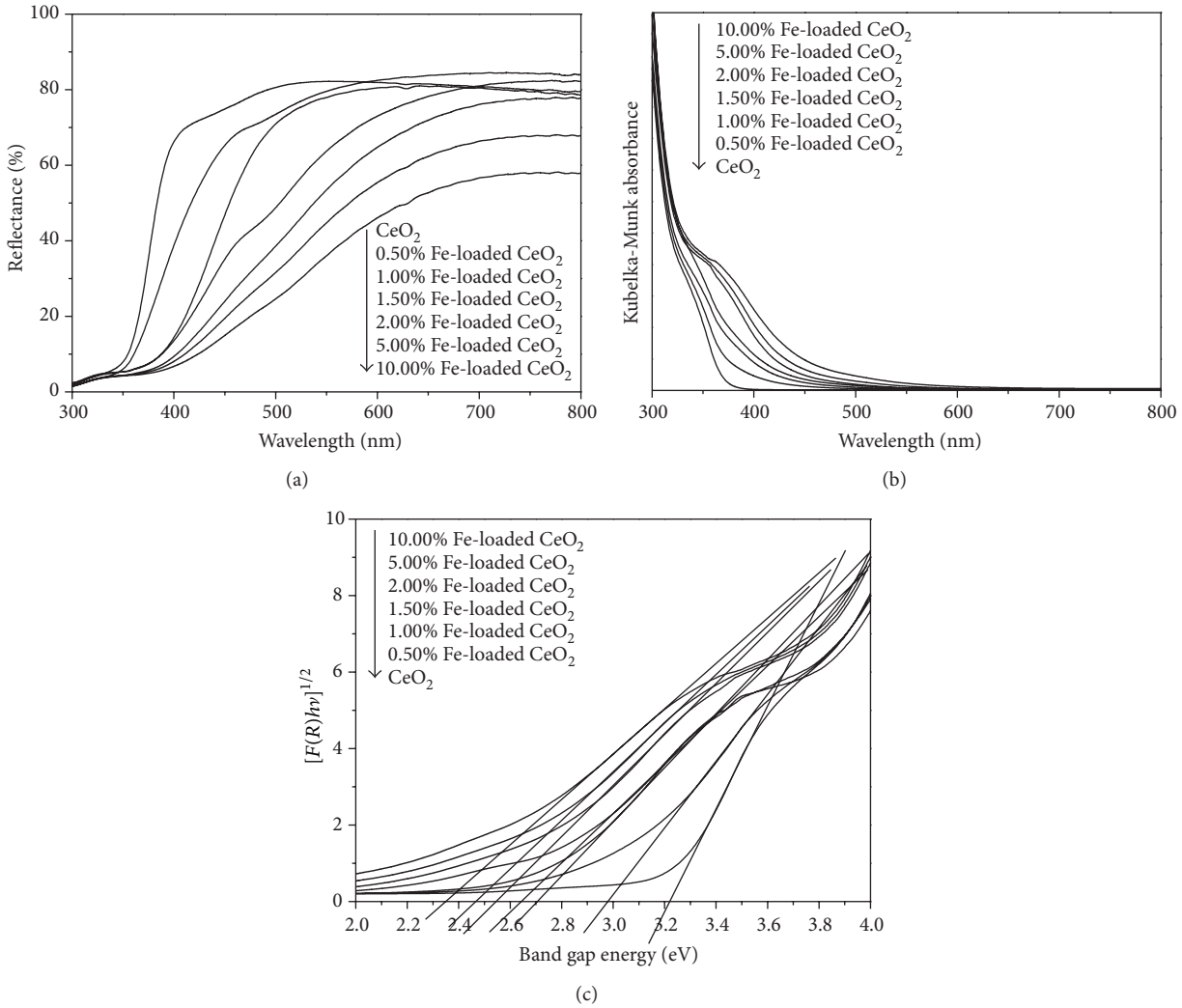

Figure 4: UV-vis (a) reflection spectra, (b) Kubelka-Munk absorbance, and (c) relation between band gap energy and $[F(R)h\nu]^{1/2}$ of CeO_2 with different iron content.

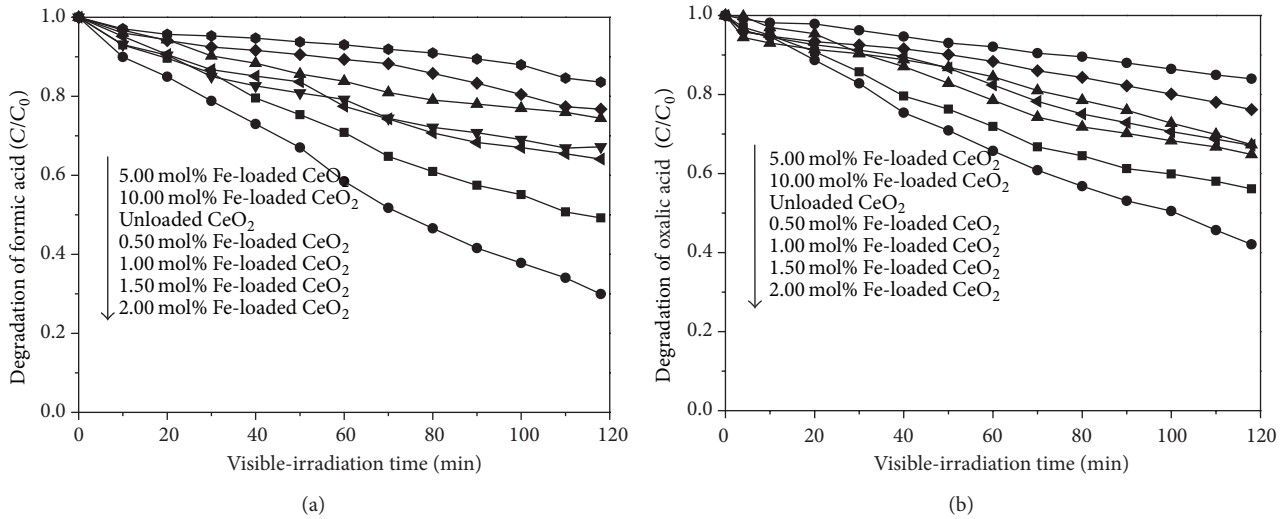

Figure 5: Photocatalytic degradation of (a) formic acid and (b) oxalic acid by CeO_2 with different iron content as a function of visible-light irradiation time.

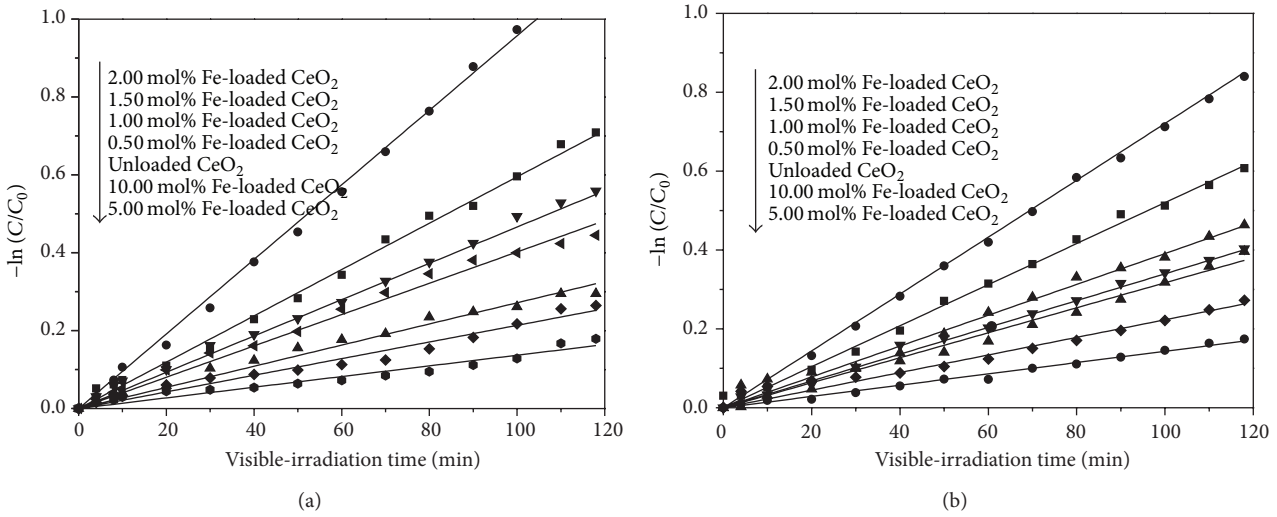

Figure 6: Kinetics plots for linear fitting of data obtained from pseudo first-order reaction for (a) formic acid and (b) oxalic acid degradation under visible-light irradiation.

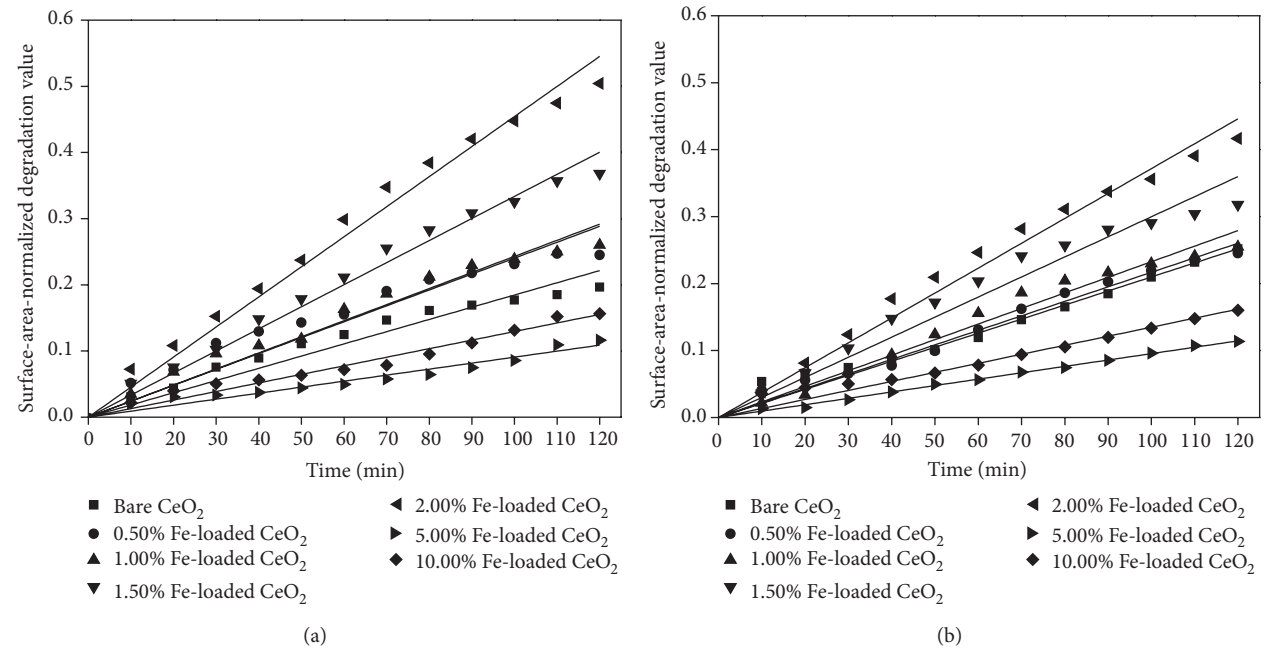

Figure 7: Kinetics plots of the surface-area-normalized degradation values against visible-light irradiation time for (a) formic acid and (b) oxalic acid.

follow pseudo first-order reaction [51] as shown in Figure 6. The pseudo first-order model is explained by

$$-\ln\left(\frac{C}{C_0}\right) = kt, \tag{4}$$

where k is the apparent rate constant (min^{-1}), C_0 means the initial concentration of acid, and C refers to the concentration of acid at various reaction times (t). The determined pseudo first-order rate constants (k, min^{-1}) are presented in Table 3. It can be seen that the loading of 2.00 mol% iron in CeO_2 nanoparticles could remarkably improve the apparent rate constant up to 5 times for formic acid and 3 times for oxalic acid compared with the unloaded one.

In order to investigate the effect of surface area on the degradation activity, the surface-area-normalized degradation values against visible-light irradiation time were plotted as shown in Figure 7, and the calculated surface-area-normalized rate constants are presented in Table 3. The results clearly suggested that surface-area of the catalyst has a crucial impact on the activity of acid degradation in this study because the surface area-normalized rate constants are significantly decreased from the original values. However, other factors such as band gap energy, amount of Fe loading,

Table 3: Apparent rate constants and surface-area-normalized rate constants.

Samples	Rate constant (k, min^{-1})		Surface-area-normalized rate constants (min^{-1} m^{-2} g)	
	Formic acid	Oxalic acid	Formic acid	Oxalic acid
5.00 mol% Fe-loaded CeO_2	0.0014	0.0014	0.0009	0.0010
10.00 mol% Fe-loaded CeO_2	0.0017	0.0020	0.0013	0.0014
Unloaded CeO_2	0.0021	0.0022	0.0019	0.0021
0.50 mol% Fe-loaded CeO_2	0.0040	0.0034	0.0024	0.0022
1.00 mol% Fe-loaded CeO_2	0.0054	0.0039	0.0024	0.0023
1.50 mol% Fe-loaded CeO_2	0.0060	0.0052	0.0033	0.0030
2.00 mol% Fe-loaded CeO_2	0.0096	0.0072	0.0045	0.0037

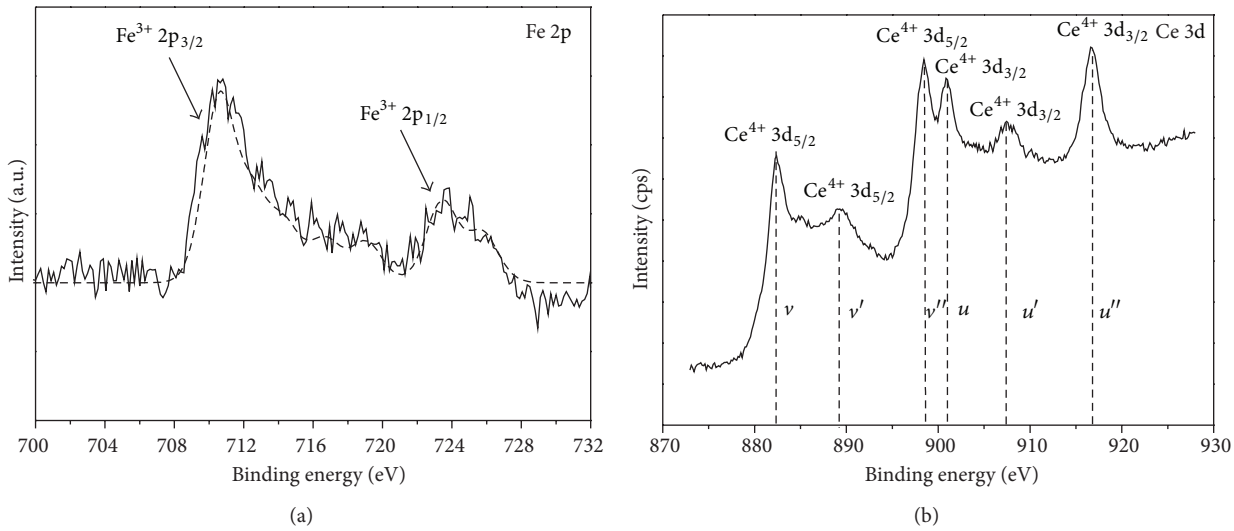

Figure 8: The XPS spectra of Fe-loaded CeO_2 nanoparticles: (a) Fe 2p and (b) Ce 3d.

sample crystallinity, and phase composition [52] could not be neglected as these could also contribute to the difference in photocatalytic activity of the catalysts being studied.

3.6. X-Ray Photoelectron Spectroscopy (XPS). In order to characterize the valence state of cerium and iron in 2.00 mol% Fe-loaded CeO_2, X-ray photoelectron spectroscopy (XPS) was carried out as shown in Figure 8.

According to Figure 8(a), the peaks at 710.6 and 723.4 eV assignable to the core level of $2p_{3/2}$ and $2p_{1/2}$, respectively, corresponded to Fe^{3+} species in Fe_2O_3 [53, 54]. No other peaks due to Fe^0 and Fe^{2+} were found in the XPS results. From the Ce 3d XPS spectrum, the binding energies of all peaks are shown in Figure 8(b). These peaks corresponded to the three pairs of spin-orbit doublets assignable to Ce^{4+} valence state which were very well in agreement with the previous reports [55, 56].

4. Conclusions

Fe-loaded CeO_2 nanoparticles with different iron loading concentrations have successfully been synthesized by flame spray pyrolysis (FSP). Loading CeO_2 with Fe^{3+} resulted in a decrease of d-spacing, lattice parameter, unit cell volume, and crystallite size but an increase of BET surface area. The UV-vis absorption spectra displayed a red shift in the band edge transition upon increasing of iron loading concentration. XPS analysis showed the presence of Fe^{3+} species on the surface of CeO_2. This could be attributed to the presence of Fe_2O_3 as observed from the XRD and HRTEM analyses. Increased photocatalytic activity compared with unloaded CeO_2 was clearly obtained from the Fe-loading sample. It was found from this study that the nominal 2.00 mol% was an optimum iron loading concentration, giving the highest photocatalytic activity. Band gap energy and surface of the catalyst were found to be important factors affecting the photocatalytic activity observed in this study. However, other factors such as amount of Fe loading, sample crystallinity, and phase composition could not be neglected.

Acknowledgments

This work has been supported by Thailand Research Fund (TRF) through the Royal Golden Jubilee (RGJ) Ph.D. Program. The National Research University Project under Thailand's Office of Higher Education Commission; the Materials Science Research Center, Department of Chemistry, Faculty of Science; and the Graduate School, Chiang Mai University, are greatly acknowledged.

References

[1] J. Nowotny, C. C. Sorrell, L. R. Sheppard, and T. Bak, "Solar-hydrogen: environmentally safe fuel for the future," *International Journal of Hydrogen Energy*, vol. 30, no. 5, pp. 521–544, 2005.

[2] T. L. Thompson and J. T. Yates Jr., "Surface science studies of the photoactivation of TiO_2-new photochemical processes," *Chemical Reviews*, vol. 106, no. 10, pp. 4428–4453, 2006.

[3] J. Zhao, C. Chen, and W. Ma, "Photocatalytic degradation of organic pollutants under visible light irradiation," *Topics in Catalysis*, vol. 35, no. 3-4, pp. 269–278, 2005.

[4] I. N. Martyanov, S. Uma, S. Rodrigues, and K. J. Klabunde, "Structural defects cause TiO_2-based photocatalysts to be active in visible light," *Chemical Communications*, vol. 10, no. 21, pp. 2476–2477, 2004.

[5] I. N. Martyanov, T. Berger, O. Diwald, S. Rodrigues, and K. J. Klabunde, "Enhancement of TiO_2 visible light photoactivity through accumulation of defects during reduction-oxidation treatment," *Journal of Photochemistry and Photobiology A*, vol. 212, no. 2-3, pp. 135–141, 2010.

[6] W. Liu and M. Flytzani-Stephanopoulos, "Transition metal-promoted oxidation catalysis by fluorite oxides: a study of CO oxidation over Cu-CeO_2," *Chemical Engineering Journal and the Biochemical Engineering Journal*, vol. 64, no. 2, pp. 283–294, 1996.

[7] G. R. Rao, J. Kašpar, S. Meriani, R. di Monte, and M. Graziani, "NO decomposition over partially reduced metallized CeO_2-ZrO_2 solid solutions," *Catalysis Letters*, vol. 24, no. 1-2, pp. 107–112, 1994.

[8] J. Kašpar, P. Fornasiero, and N. Hickey, "Automotive catalytic converters: current status and some perspectives," *Catalysis Today*, vol. 77, no. 4, pp. 419–449, 2003.

[9] Y. Li, Q. Fu, and M. Flytzani-Stephanopoulos, "Low-temperature water-gas shift reaction over Cu- and Ni-loaded cerium oxide catalysts," *Applied Catalysis B*, vol. 27, no. 3, pp. 179–191, 2000.

[10] G. Neri, A. Pistone, C. Milone, and S. Galvagno, "Wet air oxidation of p-coumaric acid over promoted ceria catalysts," *Applied Catalysis B*, vol. 38, no. 4, pp. 321–329, 2002.

[11] C. Ho, J. C. Yu, T. Kwong, A. C. Mak, and S. Lai, "Morphology-controllable synthesis of mesoporous CeO_2 nano- and microstructures," *Chemistry of Materials*, vol. 17, no. 17, pp. 4514–4522, 2005.

[12] M. I. Litter, "Heterogeneous photocatalysis: transition metal ions in photocatalytic systems," *Applied Catalysis B*, vol. 23, no. 2-3, pp. 89–114, 1999.

[13] S. Tuprakay and W. Liengcharernsit, "Lifetime and regeneration of immobilized titania for photocatalytic removal of aqueous hexavalent chromium," *Journal of Hazardous Materials*, vol. 124, no. 1–3, pp. 53–58, 2005.

[14] W. Choi, A. Termin, and M. R. Hoffmann, "The role of metal ion dopants in quantum-sized TiO_2: correlation between photoreactivity and charge carrier recombination dynamics," *Journal of Physical Chemistry*, vol. 98, no. 51, pp. 13669–13679, 1994.

[15] S. Kaur and V. Singh, "Visible light induced sonophotocatalytic degradation of reactive red dye 198 using dye sensitized TiO_2," *Ultrasonics Sonochemistry*, vol. 14, no. 5, pp. 531–537, 2007.

[16] M. Grätzel, "Photoelectrochemical cells," *Nature*, vol. 414, no. 6861, pp. 338–344, 2001.

[17] H. J. Avila-Paredes, P. Jain, S. Sen, and S. Kim, "Oxygen transport in Sc-doped CeO_2: cation (45Sc) NMR as a probe of anionic conductivity," *Chemistry of Materials*, vol. 22, no. 3, pp. 893–897, 2010.

[18] Z. Hong, H. Yoshida, and T. Sakuma, "High temperature creep strength of Si_3N_4-$Y_2Si_2O_7$ ceramics by stress relaxation based on a new interpretation model," *Key Engineering Materials*, vol. 336-338, pp. 1420–1423, 2007.

[19] P. Panagiotopoulou, J. Papavasiliou, G. Avgouropoulos, T. Ioannides, and D. I. Kondarides, "Water-gas shift activity of doped Pt/CeO_2 catalysts," *Chemical Engineering Journal*, vol. 134, no. 1–3, pp. 16–22, 2007.

[20] C. Kitiwiang and S. Phanichphant, "Synthesis of silver-doped cerium dioxide nanoparticles by the homogeneous precipitation," *Journal of Microscopy Society of Thailand*, vol. 23, no. 1, pp. 83–86, 2009.

[21] S. Maensiri, S. Phokha, P. Laokul, and S. Seraphin, "Room temperature ferromagnetism in Fe-doped CeO_2 nanoparticles," *Journal of Nanoscience and Nanotechnology*, vol. 9, no. 11, pp. 6415–6420, 2009.

[22] C. Xia, C. Hu, P. Chen, B. Wan, X. He, and Y. Tian, "Magnetic properties and photoabsorption of the Mn-doped CeO_2 nanorods," *Materials Research Bulletin*, vol. 45, no. 7, pp. 794–798, 2010.

[23] J. Sacanell, M. A. Paulin, V. Ferrari, G. Garbarino, and A. G. Leyva, "Surface photoluminescence and magnetism in hydrothermally grown undoped ZnO nanorod arrays," *Applied Physics Letters*, vol. 100, no. 11, pp. 172401–172405, 2012.

[24] S. Kumar, Y. J. Kim, B. H. Koo, and C. G. Lee, "Structural and magnetic properties of Ni doped CeO_2 nanoparticles," *Journal of Nanoscience and Nanotechnology*, vol. 10, no. 11, pp. 7204–7207, 2010.

[25] T. S. Santos, W. S. D. Folly, and M. A. Macêdo, "Ferromagnetism in diluted magnetic Zn-Co-doped $CeO_{2-\delta}$," *Physica B: Condensed Matter*, vol. 407, no. 16, pp. 3233–3235, 2012.

[26] J. Araña, O. González Díaz, M. Miranda Saracho, J. M. Doa Rodríguez, J. A. Herrera Melián, and J. Pérez Pea, "Photocatalytic degradation of formic acid using Fe/TiO_2 catalysts: the role of Fe^{3+}/Fe^{2+} ions in the degradation mechanism," *Applied Catalysis B*, vol. 32, no. 1-2, pp. 49–61, 2001.

[27] Q.-Z. Yan, X.-T. Su, Z.-Y. Huang, and C.-C. Ge, "Sol-gel auto-igniting synthesis and structural property of cerium-doped titanium dioxide nanosized powders," *Journal of the European Ceramic Society*, vol. 26, no. 6, pp. 915–921, 2006.

[28] L. Yin, Y. Wang, G. Pang, Y. Koltypin, and A. Gedanken, "Sonochemical synthesis of cerium oxide nanoparticles—effect of additives and quantum size effect," *Journal of Colloid and Interface Science*, vol. 246, no. 1, pp. 78–84, 2002.

[29] L. Truffault, Q. W. Yao, D. Wexler et al., "Synthesis and characterization of Fe doped CeO_2 nanoparticles for pigmented ultraviolet filter applications," *Journal of Nanoscience and Nanotechnology*, vol. 11, no. 5, pp. 4019–4028, 2011.

[30] M. Hirano and M. Inagaki, "Preparation of monodispersed cerium(IV) oxide particles by thermal hydrolysis: influence of the presence of urea and Gd doping on their morphology and growth," *Journal of Materials Chemistry*, vol. 10, no. 2, pp. 473–477, 2000.

[31] A. Bumajdad, M. I. Zaki, J. Eastoe, and L. Pasupulety, "Microemulsion-based synthesis of CeO_2 powders with high surface area and high-temperature stabilities," *Langmuir*, vol. 20, no. 25, pp. 11223–11233, 2004.

[32] D. Terribile, A. Trovarelli, J. Llorca, C. De Leitenburg, and G. Dolcetti, "The synthesis and characterization of mesoporous

high-surface area ceria prepared using a hybrid organic/inorganic route," *Journal of Catalysis*, vol. 178, no. 1, pp. 299–308, 1998.

[33] L. Mädler, W. J. Stark, and S. E. Pratsinis, "Flame-made ceria nanoparticles," *Journal of Materials Research*, vol. 17, no. 6, pp. 1356–1362, 2002.

[34] R. Mueller, L. Mädler, and S. E. Pratsinis, "Nanoparticle synthesis at high production rates by flame spray pyrolysis," *Chemical Engineering Science*, vol. 58, no. 10, pp. 1969–1976, 2003.

[35] L. Mädler, T. Sahm, A. Gurlo et al., "Sensing low concentrations of CO using flame-spray-made Pt/SnO_2 nanoparticles," *Journal of Nanoparticle Research*, vol. 8, no. 6, pp. 783–796, 2006.

[36] T. Samerjai, N. Tamaekonga, K. Wetchakun et al., "Flame-spray-made metal-loaded semiconducting metal oxides thick films for flammable gas sensing," *Sensors and Actuators B*, vol. 171-172, pp. 43–61, 2012.

[37] C. Liewhiran and S. Phanichphant, "Effects of palladium loading on the response of a thick film flame-made ZnO gas sensor for detection of ethanol vapor," *Sensors*, vol. 7, no. 7, pp. 1159–1184, 2007.

[38] B. Li, X. Wang, M. Yan, and L. Li, "Preparation and characterization of nano-TiO_2 powder," *Materials Chemistry and Physics*, vol. 78, no. 1, pp. 184–188, 2003.

[39] A. Gupta, M. S. Hegde, K. R. Priolkar, U. V. Waghmare, P. R. Sarode, and S. Emura, "Structural investigation of activated lattice oxygen in $Ce_{1-x}Sn_xO_2$ and $Ce_{1-x-y}Sn_xPdyO_{2-\delta}$ by EXAFS and DFT calculation," *Chemistry of Materials*, vol. 21, no. 24, pp. 5836–5847, 2009.

[40] T. Nishimura, H. Katayama, K. Noda, and T. Kodama, "Electrochemical behavior of rust formed on carbon steel in a wet/dry environment containing chloride ions," *Corrosion*, vol. 56, no. 9, pp. 935–941, 2000.

[41] R. D. Shannon, "Revised effective ionic radii and systematic studies of interatomie distances in halides and chaleogenides," *Acta Crystallographica Section A*, vol. 32, no. 5, pp. 751–767, 1976.

[42] G. L. Beausoleil, A. Thurber, S. S. Rao, G. Alanko, C. B. Hanna, and A. Punnoose, "Concentration dependence of magnetic moment in $Ce_{1-x}Fe_xO_2$," *Journal of Applied Physics*, vol. 111, no. 7, pp. 1–9, 2012.

[43] N. Wu, L. Chen, Y. Jiao, G. Chen, and J. Li, "Preparation and characterization of Fe^{3+}, La^{3+} Co-doped TiO_2 nanofibers and its photocatalytic activity," *Journal of Engineered Fibers and Fabrics*, vol. 7, no. 3, pp. 16–20, 2012.

[44] L. Wen, B. Liu, X. Zhao, K. Nakata, T. Murakami, and A. Fujishima, "Synthesis, characterization, and photocatalysis of Fe-doped TiO_2: a combined experimental and theoretical study," *International Journal of Photoenergy*, vol. 2012, Article ID 368750, 10 pages, 2012.

[45] S. Agarwala, M. Kevin, A. S. W. Wong, C. K. N. Peh, V. Thavasi, and G. W. Ho, "Mesophase ordering of TiO_2 film with high surface area and strong light harvesting for dye-sensitized solar cell," *ACS Applied Materials and Interfaces*, vol. 2, no. 7, pp. 1844–1850, 2010.

[46] J. Sirita, S. Phanichphant, and F. C. Meunier, "Quantitative analysis of adsorbate concentrations by diffuse reflectance FT-IR," *Analytical Chemistry*, vol. 79, no. 10, pp. 3912–3918, 2007.

[47] G. Wang, L. Xu, J. Zhang, T. Yin, and D. Han, "Enhanced photocatalytic activity of TiO_2 powders (P25) via calcination treatment," *International Journal of Photoenergy*, vol. 2012, Article ID 265760, 9 pages, 2012.

[48] P. R. Mishra and O. N. Srivastava, "On the synthesis, characterization and photocatalytic applications of nanostructured TiO_2," *Bulletin of Materials Science*, vol. 31, no. 3, pp. 545–550, 2008.

[49] M. K. Seery, R. George, P. Floris, and S. C. Pillai, "Silver doped titanium dioxide nanomaterials for enhanced visible light photocatalysis," *Journal of Photochemistry and Photobiology A*, vol. 189, no. 2-3, pp. 258–263, 2007.

[50] Z. Zhang, C.-C. Wang, R. Zakaria, and J. Y. Ying, "Role of particle size in nanocrystalline TiO_2-based photocatalysts," *Journal of Physical Chemistry B*, vol. 102, no. 52, pp. 10871–10878, 1998.

[51] A. Olad, S. Behboudi, and A. A. Entezami, "Preparation, characterization and photocatalytic activity of TiO_2/polyaniline core-shell nanocomposite," *Bulletin of Materials Science*, vol. 35, no. 5, pp. 801–809, 2012.

[52] Y. Mizukoshi and N. Masahashi, "Photocatalytic activities and crystal structures of titanium dioxide by anodization: their dependence upon current density," *Materials Transactions*, vol. 51, no. 8, pp. 1443–1448, 2010.

[53] T. Yamashita and P. Hayes, "Analysis of XPS spectra of Fe^{2+} and Fe^{3+} ions in oxide materials," *Applied Surface Science*, vol. 254, no. 8, pp. 2441–2449, 2008.

[54] A. P. Grosvenor, B. A. Kobe, M. C. Biesinger, and N. S. McIntyre, "Investigation of multiplet splitting of Fe 2p XPS spectra and bonding in iron compounds," *Surface and Interface Analysis*, vol. 36, no. 12, pp. 1564–1574, 2004.

[55] G. K. Pradhan and K. M. Parida, "Fabrication of iron-cerium mixed oxide: an efficient photocatalyst for dye degradation," *International Journal of Engineering Science and Technology*, vol. 2, no. 9, pp. 53–65, 2010.

[56] A. Khare, R. J. Choudhary, K. Bapna, D. M. Phase, and S. P. Sanyal, "Resonance photoemission studies of (111) oriented CeO_2 thin film grown on Si (100) substrate by pulsed laser deposition," *Journal of Applied Physics*, vol. 108, no. 10, Article ID 103712, 2010.